Journal of
Applied
Crystallography
ISSN 1600-5767

Received 14 October 2013
Accepted 14 March 2014

Connecting heterogeneous single slip to diffraction peak evolution in high-energy monochromatic X-ray experiments

Darren C. Pagan and Matthew P. Miller*

Sibley School of Mechanical and Aerospace Engineering, Cornell University and Cornell High Energy Synchrotron Source, Ithaca, NY, USA. Correspondence e-mail: mpm4@cornell.edu

A forward modeling diffraction framework is introduced and employed to identify slip system activity in high-energy diffraction microscopy (HEDM) experiments. In the framework, diffraction simulations are conducted on virtual mosaic crystals with orientation gradients consistent with Nye's model of heterogeneous single slip. Simulated diffraction peaks are then compared against experimental measurements to identify slip system activity. Simulation results compared against diffraction data measured *in situ* from a silicon single-crystal specimen plastically deformed under single-slip conditions indicate that slip system activity can be identified during HEDM experiments.

1. Introduction

The ability to produce high-flux high-energy monochromatic X-ray beams, in addition to area detectors with rapid collection times, is enabling a new generation of *in situ* characterization experiments for crystalline materials. High-energy diffraction microscopy (HEDM) techniques allow for the study of deformation of polycrystalline engineering materials at the crystal scale where the origins of failure modes such as fatigue and fracture occur. Generally, these experiments are rotating crystal diffraction experiments, conducted in a transmission geometry, with an area detector placed behind the sample. The distribution of intensity of each diffraction peak contains information about both the real-space topology and the lattice state of the grains (Poulsen, 2004). The lattice state is described by the local lattice orientation, lattice strain and dislocation density, which can vary across the crystal. HEDM experiments are usually classified according to the sample-to-detector distance: near-field experiments, where the area detector is close to the sample (Li *et al.*, 2012; Johnson *et al.*, 2008); far-field (Poulsen, 2004; Margulies *et al.*, 2002; Lienert *et al.*, 2009) [or very far-field (Jakobsen *et al.*, 2006)] experiments, where the detector is far from the sample; and intermediate field, where the detector sits between these two extremes. Near-field experiments tend to be sensitive to the real-space topology of grains within a sample, while far-field experiments are more sensitive to the reciprocal-space distributions of lattice strain and orientation within grains. In intermediate-field geometries, diffraction data are equally sensitive to the real-space topology and the reciprocal space of the crystal. The high-energy stations at the Cornell High Energy Synchrotron Source (CHESS) are currently well suited to conduct intermediate- and far-field HEDM experiments. Once the diffraction data have been collected, the methods of interpreting the data fall under two broad categories: forward modeling (Suter *et al.*, 2006; Ludwig *et al.*, 2009; Wong *et al.*, 2013; Gonzalez *et al.*, 2013) and direct inversion (Poulsen, 2004; Bernier *et al.*, 2011). Forward-modeling techniques use models to completely represent the material, then simulate conditions of the diffraction experiment in order to generate synthetic diffraction data, which can be directly compared with experimental results. Inversion techniques use models to process diffraction data to determine quantities of interest such as lattice strain or orientation. In this work, a new forward modeling technique is presented to be used to determine slip system activity within deforming crystals at the onset of plastic deformation using diffraction data from intermediate- and far-field geometries. This analysis will allow for new information about plasticity to be gathered at the crystal scale from HEDM techniques.

During the plastic deformation of crystalline materials, the lattice state evolves, subsequently changing the mechanical response of the crystal. The most prevalent mechanism of plastic deformation is dislocation glide (slip) upon a specific slip system or sets of slip systems. Dislocation glide occurs when a sufficient shear stress is resolved upon the slip system, allowing lattice planes to move relative to one another. In diffraction images from deforming crystals, the change in state is reflected in changes of the distribution of diffracted intensity measured on a detector. Observations of sets of diffraction peaks from plastically deformed crystals using both monochromatic and polychromatic X-ray beams have shown that diffraction peaks from different sets of lattice planes evolve by varying amounts (Joffe & Kirpitcheva, 1922; Cahn, 1950; Lienert *et al.*, 2009), with the evolution dictated by the specific distributions of state in the crystal. The observed peak evolution is due to the distribution of the lattice state developing within the crystal as dislocation glide proceeds. Simply put, the regions of different lattice state within the crystal diffract X-rays to different regions on the detector, changing the distribution of diffracted intensity.

In order to identify slip system activity from measured diffraction peak evolution, a model that relates the two is necessary. Nye (1953) showed that heterogeneous slip will cause the lattice to develop orientation gradients, which depend on which slip systems were active. This is due to unpaired dislocations of a single sign [geometrically necessary dislocations (GNDs)] accumulating on the slip plane, causing the lattice to develop an orientation gradient. Work using polychromatic X-rays has shown that orientation gradients due to single slip produce characteristic streaking of Laue diffraction peaks. This streaking can be related to slip system activity (Barabash *et al.*, 2001, 2003; Ice & Barabash, 2007; Van Swygenhoven & Petegem, 2010), while forward modeling can be used to further analyze the diffraction peak streaking to understand dislocation activity and lattice misorientation (Song *et al.*, 2010; Hofmann *et al.*, 2012; Korsunsky *et al.*, 2012; Wong *et al.*, 2013). In monochromatic X-ray experiments, the diffraction peak evolution due to a distribution of orientation is 'orthogonal' to broadening due to a distribution of lattice strain (in the azimuthal and radial directions, respectively, of a detector behind the sample). In previous work, monochromatic X-rays were used to analyze the broadening of rocking curves (distributions of intensity in reciprocal space orthogonal to the distributions of intensity studied in traditional line broadening experiments) due to misorientation in a copper single crystal plastically deformed *ex situ*. The broadening was subsequently related to the GND configuration present within the crystal (Wilkens *et al.*, 1987). This would all indicate that, by analyzing diffraction peak evolution due to misorientation in intermediate- and far-field geometries using forward modeling, one should be able to ascertain slip system activity. In this paper, diffraction experiments and simulations were conducted on silicon single crystals oriented for single slip during uniaxial compression. By conducting an experiment where the active slip system is known, the utility of the method can be tested.

This paper is organized as follows: §2 provides a description of how diffraction from a crystal with an orientation gradient causes azimuthal broadening on an area detector behind the sample and how the position of the detector affects the data collected; §3.1 describes the process of generating virtual deformed single crystals, and §3.2 describes how synthetic diffraction images are generated; §4 compares simulated diffraction results with an experiment conducted on a silicon crystal plastically deformed at 1073 K; and the applicability of the model and the results are discussed in §5. In the following work, bold characters will indicate vectors ($\mathbf{a}$), and bold underlined characters will represent second-rank tensors ($\underline{\mathbf{a}}$). Italic characters will indicate scalar variables and Roman characters vector/tensor components. The vectors $\mathbf{x}$, $\mathbf{y}$ and $\mathbf{z}$ will be reserved for rectangular Cartesian coordinate system directions. Superscripts will denote the coordinate systems in which vectors or tensors are expressed ($\mathbf{a}^{\mathrm{S}}$). Boldface subscripts will generally identify specific vectors or tensors ($\mathbf{a_0}$), while plainface subscripts will indicate vector or tensor components (a_x or a_{xx}). Lastly, carats will indicate unit vectors ($\hat{\mathbf{a}}$).

2. Background

In this section, the changes in diffracted intensity distributions in HEDM experiments due to lattice misorientation in crystals will be described. A mosaic crystal model is employed to describe diffraction from a deformed crystal because the effects of both topology and distributions of orientation are readily included in the diffraction description. In the mosaic model, the deformed crystal is divided into crystallites (mosaic blocks), which are small regions of crystal with uniform state (Darwin, 1914). In the model, the divisions between blocks are distinct and there is no interaction between diffracted beams from different mosaic blocks. Therefore, diffraction from each block can be described using the kinematic description of diffraction from a small crystallite. The mosaic model is appropriate for describing crystals with distributions of state present, such as grains within a polycrystal or large crystals with distributions of state (Warren, 2004). Each diffraction 'peak' measured from a mosaic crystal becomes a summation of diffracted intensity from all the mosaic blocks, and the intensity distribution of diffraction peaks from a mosaic crystal therefore depends on the positions and states of all the mosaic blocks.

Diffraction events are most easily described using reciprocal-lattice vectors ($\mathbf{g}_{hkl}$),

$$\mathbf{g}_{hkl} = h\mathbf{b_1} + k\mathbf{b_2} + l\mathbf{b_3}, \tag{1}$$

where h, k and l are integers used to identify the set of lattice planes corresponding to the reciprocal-lattice vector. The reciprocal lattice basis vectors ($\mathbf{b_1}$, $\mathbf{b_2}$, $\mathbf{b_3}$) are constructed using the crystal lattice basis vectors (Warren, 2004). While most easily expressed in the crystal coordinate system ($\mathbf{x}^{\mathrm{C}}$, $\mathbf{y}^{\mathrm{C}}$, $\mathbf{z}^{\mathrm{C}}$), reciprocal-lattice vectors are measured with respect to the laboratory coordinate system ($\mathbf{x}^{\mathrm{L}}$, $\mathbf{y}^{\mathrm{L}}$, $\mathbf{z}^{\mathrm{L}}$). A rotation matrix, $\underline{\mathbf{R}}^{\mathrm{L,C}}$, is defined, which transforms $\mathbf{g}_{hkl}$ from the crystal to the laboratory coordinate system:

$$\mathbf{g}^{\mathrm{L}}_{hkl} = \underline{\mathbf{R}}^{\mathrm{L,C}}\mathbf{g}^{\mathrm{C}}_{hkl}. \tag{2}$$

During the diffraction experiment, the sample is rotated with respect to the laboratory coordinate system, seen in Fig. 1(*a*). Since the sample is reoriented during the experiment, evolution of $\mathbf{g}_{hkl}$ during deformation is more easily understood with respect to the sample coordinate system ($\mathbf{x}^{\mathrm{S}}$, $\mathbf{y}^{\mathrm{S}}$, $\mathbf{z}^{\mathrm{S}}$). To take into account the orientation of the crystal relative to the sample, the rotation matrix $\underline{\mathbf{R}}^{\mathrm{L,C}}$ is further decomposed into

$$\underline{\mathbf{R}}^{\mathrm{L,C}} = \underline{\mathbf{R}}^{\mathrm{L,S}}\underline{\mathbf{R}}^{\mathrm{S,C}}. \tag{3}$$

Physically, $\underline{\mathbf{R}}^{\mathrm{L,S}}$ is a reorientation of the sample by a diffractometer, while $\underline{\mathbf{R}}^{\mathrm{S,C}}$ is the orientation of the crystal lattice with respect to the sample coordinate system, which is fixed to known sample features.

Monochromatic X-rays can be described as plane waves with a wavevector, $\mathbf{k}$, which holds information about the wavelength of the X-ray, λ, and the direction of propagation, $\hat{\mathbf{k}}$. Diffraction from a crystal is typically parameterized by the scattering vector, $\mathbf{q}$, which is the difference in wavevectors of the diffracted, $\mathbf{k_o}$, and incoming, $\mathbf{k_i}$, X-ray beams:

$$\mathbf{q} = \mathbf{k_o} - \mathbf{k_i}. \tag{4}$$

Diffraction occurs when a reciprocal-lattice vector is equal to the scattering vector (Warren, 2004),

$$\mathbf{q} = \mathbf{g}_{hkl}, \tag{5}$$

with the constraint that the scattering is elastic:

$$\|\mathbf{k_i}\| = \|\mathbf{k_o}\| = \|\mathbf{k_i} + \mathbf{q}\|. \tag{6}$$

The intensity, I, of the diffracted X-ray beam in a kinematic description of diffraction (Als-Nielsen & McMorrow, 2011) is given by

$$I(\mathbf{q}) = \Phi r_0^2 N v' \sum_{\mathbf{g}_{hkl}} \|F(\mathbf{q})\|^2 \delta(\mathbf{q} - \mathbf{g}_{hkl}), \tag{7}$$

where Φ is the flux of the incoming X-ray beam, r_0 is the classical electron radius, N is the number of unit cells illuminated, v' is the volume of a reciprocal-lattice unit cell, $F(\mathbf{q})$ describes the scattering from a unit cell as a function of $\mathbf{q}$ and δ is the Dirac delta function. The kinematic description of diffraction requires the crystallite to be 'small' so that neither the incoming nor diffracted X-ray beams are appreciably attenuated as they pass through the crystallite. Small is a relative term which varies depending on the X-ray energy, the material and the set of lattice planes that is diffracting, but the upper limit is generally hundreds of micrometres (Authier, 2001). For use in a mosaic crystal model, this attenuation length defines the upper limit of the characteristic length of a mosaic block. The dependence of the diffracted intensity on the number of diffracting unit cells (N) implies that the intensity of a diffraction peak is proportional to the crystallite volume (Warren, 2004).

In a rotating crystal experiment, illustrated in Fig. 1(*a*), the diffractometer rotates a sample about a single axis that is perpendicular to the incoming monochromatic X-ray beam as the sample is illuminated. An area detector, positioned a distance D behind the sample, collects intensity from sets of lattice planes as their corresponding reciprocal-lattice vectors diffract. The laboratory coordinate system is defined so that the incoming beam travels in the $-\mathbf{z}^{\mathrm{L}}$ direction and the rotation axis lies in the $\mathbf{y}^{\mathrm{L}}$ direction. In this configuration, $\underline{\mathbf{R}}^{\mathrm{L,S}}$ is given by

$$\underline{\mathbf{R}}^{\mathrm{L,S}} = \begin{bmatrix} \cos(\omega) & 0 & \sin(\omega) \\ 0 & 1 & 0 \\ -\sin(\omega) & 0 & \cos(\omega) \end{bmatrix}. \tag{8}$$

The origins of both laboratory and sample coordinate systems are the intersection of the incoming X-ray beam and the rotation axis of the diffractometer. The center of the detector is aligned with the incoming beam, while the detector face is perpendicular to the beam propagation direction, $\hat{\mathbf{k}}_\mathbf{i}$. The two-dimensional coordinate system directions on the detector ($\mathbf{x}^{\mathrm{DET}}$, $\mathbf{y}^{\mathrm{DET}}$) are chosen to be parallel to $\mathbf{x}^{\mathrm{L}}$ and $\mathbf{y}^{\mathrm{L}}$, respectively, with the origin at the detector center. Measured diffraction peaks are parameterized by the angles 2θ, η and ω. The angle 2θ is determined from the radial position of the diffraction peak and D, η is the azimuthal angle measured counterclockwise from $\mathbf{x}^{\mathrm{DET}}$, and ω is the diffractometer angle when the diffraction event occurred. In practice, the sample rotates across a fixed angular interval, $\Delta\omega$, as the detector collects (integrates) all diffracted intensity from the interval onto a single image. The indicated value of ω of each diffraction peak then becomes the center of $\Delta\omega$, where the diffraction peak is observed. In this experimental configuration, when $\mathbf{g}_{hkl}$ rotates about $\mathbf{y}^{\mathrm{L}}$, $\mathbf{g}_{hkl}$ can satisfy the diffraction condition zero, one or two times depending on its magnitude and orientation as the diffractometer rotates (Busing & Levy, 1967). The diffraction peaks appear on different projected Debye–Scherrer rings depending on $\|\mathbf{g}_{hkl}\|$. Most importantly for this work, changes in the orientation of the crystal with respect to the sample will change the angles η and ω at which diffraction peaks occur. If the usual practice of completely integrating the diffraction peak by rotating the diffractometer (integrating the ω parameterization of the diffraction peak) is performed, changes in orientation can only be indicated by azimuthal shifts (changes in η) of the peak on the detector.

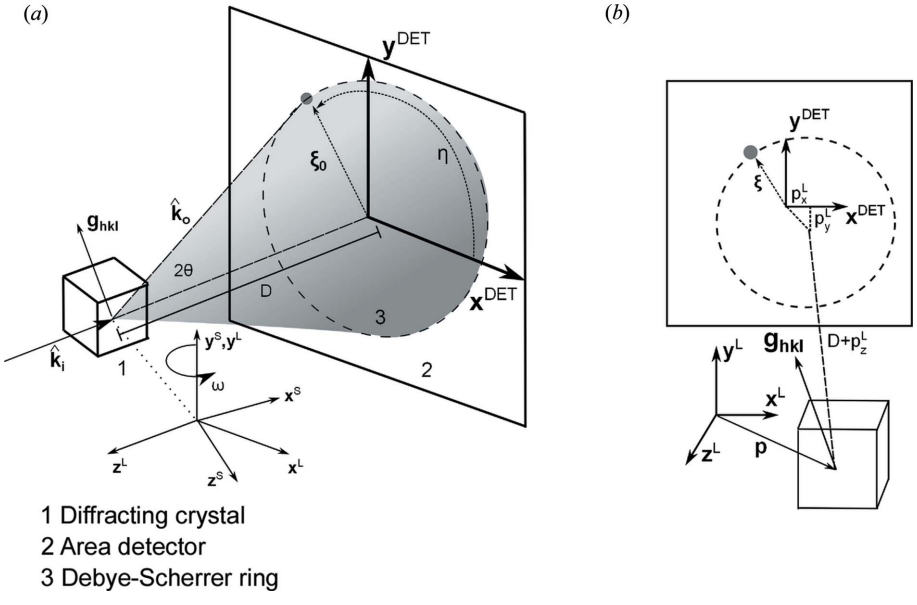

Figure 1
(*a*) A diffraction event in a rotating crystal experiment geometry. The measured diffraction peak is parameterized by the angles 2θ and η on the detector where it is measured, and the diffractometer angle, ω. The intercept of a diffracted beam from a mosaic block centered at the laboratory origin with the detector is ξ_0, and D is the sample-to-detector distance. (*b*) A diffraction event from a mosaic block that is not centered at the laboratory coordinate system origin. The position, $\mathbf{p}$, is a vector from the crystal center to the laboratory coordinate system origin. The intercept of the diffracted beam from a mosaic block not centered at the laboratory origin with the detector is ξ.

If a mosaic block is located at the laboratory origin, the two-dimensional detector intercept, $\boldsymbol{\xi_0}$, of a beam diffracted in the $\hat{\mathbf{k}}_\mathbf{o}$ direction can be found by solving the set of equations

$$C\begin{bmatrix}\hat{\mathbf{k}}^{\mathrm{L}}_{\mathbf{ox}}\\ \hat{\mathbf{k}}^{\mathrm{L}}_{\mathbf{oy}}\\ \hat{\mathbf{k}}^{\mathrm{L}}_{\mathbf{oz}}\end{bmatrix}=\begin{bmatrix}\xi_{\mathbf{0x}}\\ \xi_{\mathbf{0y}}\\ -D\end{bmatrix}, \tag{9}$$

where C is an unknown scaling constant. Solving these equations for $\boldsymbol{\xi_0}$ gives

$$\boldsymbol{\xi_0}=\begin{bmatrix}-(\hat{\mathbf{k}}^{\mathrm{L}}_{\mathbf{ox}}/\hat{\mathbf{k}}^{\mathrm{L}}_{\mathbf{oz}})D\\ -(\hat{\mathbf{k}}^{\mathrm{L}}_{\mathbf{oy}}/\hat{\mathbf{k}}^{\mathrm{L}}_{\mathbf{oz}})D\end{bmatrix}. \tag{10}$$

Since most mosaic blocks in a crystal are not centered at the laboratory origin, the position $\mathbf{p}$ must be accounted for when calculating the general detector intercept, $\boldsymbol{\xi}$ (Poulsen, 2004). Fig. 1(*b*) illustrates a diffraction event from a mosaic block that is illuminated but not centered on the origin of the laboratory coordinate system. The position of the mosaic block has two primary effects on the detector intercept. First, the components of $\mathbf{p}$ transverse to the beam ($\mathrm{p}^{\mathrm{L}}_{\mathrm{x}}$ and $\mathrm{p}^{\mathrm{L}}_{\mathrm{y}}$) during the diffraction event displace the intercept between diffracted beam and detector. Second, the position of the mosaic block along the beam direction ($\mathrm{p}^{\mathrm{L}}_{\mathrm{z}}$) changes the distance from the mosaic block to the detector, which in turn shifts the radial position of the peak on the detector. Considering these effects, detector intercepts of diffracted X-rays from a precessing mosaic block are given by

$$\boldsymbol{\xi}=\boldsymbol{\xi}_0+\begin{bmatrix}\mathrm{p}^{\mathrm{L}}_{\mathrm{x}}-(\hat{\mathbf{k}}^{\mathrm{L}}_{\mathbf{ox}}/\hat{\mathbf{k}}^{\mathrm{L}}_{\mathbf{oz}})\mathrm{p}^{\mathrm{L}}_{\mathrm{z}}\\ \mathrm{p}^{\mathrm{L}}_{\mathrm{y}}-(\hat{\mathbf{k}}^{\mathrm{L}}_{\mathbf{oy}}/\hat{\mathbf{k}}^{\mathrm{L}}_{\mathbf{oz}})\mathrm{p}^{\mathrm{L}}_{\mathrm{z}}\end{bmatrix}, \tag{11}$$

where $\boldsymbol{\xi_0}$ is the detector intercept if the mosaic block is centered at the laboratory origin. The first term on each row accounts for the transverse position of the mosaic block, while the second term accounts for the position of the mosaic block along the beam direction during the diffraction event. Note that by increasing D, the detector intercept will transition from being position dominant (bracket term) to being dominated by the direction of propagation of the diffracted beam ($\boldsymbol{\xi_0}$).

As mentioned previously, the spatial distribution of diffracted intensity from a mosaic crystal measured at the detector is a combination of the topology and the distribution of lattice state, so care must be taken when interpreting changes as solely related to changing lattice state distributions. Fig. 2 illustrates the competing effects of the topology of the mosaic blocks *versus* distribution of orientation. As described in Fig. 1(*b*), the position of each mosaic block plays a roll in determining where the diffracted beam intercepts the detector. The effect of the topology of the mosaic blocks on the diffracted intensity is observed as the shape of the diffraction volume projected on to the detector. The effect of the topology on the diffracted intensity can be simply quantified by a characteristic diffraction volume length, $\|\Delta\mathbf{p}\|$, which roughly describes the total projected size of a diffracting volume. This could be the diameter of a fully illuminated grain in a polycrystal or the size of the beam illuminating a large crystal. The effect of misorientation on diffracted intensity will be characterized by the spreading of diffraction peaks along an azimuthal arc, $\Delta\eta$, if the mosaic blocks are all located at an idealized source point, a distance D from the detector. The length of this arc on the detector is given by

$$\Delta\eta=\Delta R_{hkl}D\tan(2\theta), \tag{12}$$

where ΔR_{hkl} describes the magnitude of the angular misorientation of $\mathbf{g}_{hkl}$ from all mosaic blocks. In Fig. 2, this corresponds to the angle between $\mathbf{g}_{hkl\mathbf{1}}$ and $\mathbf{g}_{hkl\mathbf{3}}$. From equation (12), it can be seen that the spreading of the arc increases with the angle 2θ and D. It should be noted that $\Delta\eta$ is an approximate measure of the azimuthal peak spreading since reorientation of $\mathbf{g}_{hkl}$ in the same direction that the diffractometer rotates (about $\mathbf{y}^{\mathrm{L}}$) will not be observed in these experiments. Fig. 2 illustrates that, by adjusting the detector distance, the diffracted intensity distribution from a set of misoriented mosaic blocks will change from being dominated by the topology of the mosaic blocks (near field), to the effects being about equal (intermediate field), to the diffracted intensity being dominated by the misorientation of the mosaic blocks (far field). As the detector distance increases, the $\boldsymbol{\xi}$ of diffracted beams from each mosaic block appear on a single azimuthal arc as $\boldsymbol{\xi_0}$ becomes dominant. These changes to the

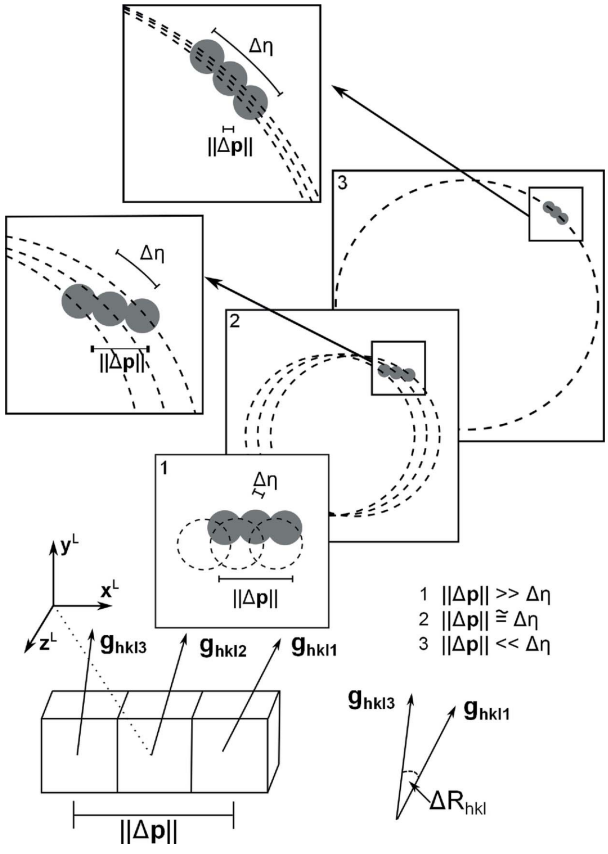

Figure 2
Three misoriented mosaic blocks forming a mosaic crystal. The mosaic blocks have diffracted as the mosaic crystal rotated about $\mathbf{y}^{\mathrm{L}}$. The distribution of diffracted intensity on the detector evolves with changing sample-to-detector distance.

observed diffracted intensity with changing detector distance are the fundamental differences between near-field ($\|\Delta\mathbf{p}\| << \eta$) and far-field ($\|\Delta\mathbf{p}\| >> \eta$) diffraction measurements (Poulsen, 2004).

3. Modeling deformed crystals and resulting diffraction peaks

A framework for simulating diffraction experiments using virtual mosaic crystals is presented in this section. The goal of the framework is to determine the azimuthal peak width evolution related to misorientation caused by heterogeneous single slip, which can then be compared with experimental data. The framework uses a simple, but flexible, method to generate virtual mosaic crystals with orientation gradients consistent with heterogeneous single slip at the onset of plastic deformation. Crystal orientation fields, present at the continuum size scale in the model, are approximated by discrete rotations of individual mosaic blocks. The total misorientation present within the mosaic crystals is less than 1°, consistent with the onset of plastic deformation.

3.1. Generating virtual silicon samples

Nye's model for heterogeneous slip during dislocation glide is implemented. The model predicts that the slip plane and the entire lattice develop a gradient of orientation and, subsequently, curvature (Nye, 1953; Arsenlis & Parks, 1999). In this model, the curvature due to the elastic deformation gradient is assumed to be negligible (Nye, 1953). The left side of Fig. 3 shows a two-dimensional schematic of a virtual mosaic crystal with a uniform initial distribution of orientation prior to the application of an orientation gradient. Each virtual crystal is discretized into a collection of equally spaced volumes which serve as mosaic blocks, where each mosaic block has an orientation, $\underline{\mathbf{R}}^{S,C}$, dependent on its position within the crystal, $\mathbf{p}$ (Fig. 1*b*), which is consistent with Nye's model.

The orientation field, $\underline{\mathbf{R}}^{S,C}(\mathbf{p})$, in the mosaic crystal is decomposed into a small position-dependent orientation perturbation, $\underline{\mathbf{R}}_{\varphi}(\mathbf{p})$, from an initial crystal orientation $\underline{\mathbf{R}}_{\mathbf{0}}{}^{S,C}$

$$\underline{\mathbf{R}}^{S,C}(\mathbf{p}) = \underline{\mathbf{R}}_{\varphi}(\mathbf{p})\underline{\mathbf{R}}_{\mathbf{0}}{}^{S,C}. \tag{13}$$

At the onset of plastic deformation, the orientation perturbations are small, so $\underline{\mathbf{R}}_{\varphi}$ can be described as an infinitesimal rotation which is additively decomposed into

$$\underline{\mathbf{R}}_{\varphi} = \underline{\mathbf{I}} + \text{skew}(\boldsymbol{\varphi}), \tag{14}$$

where $\boldsymbol{\varphi}$ is an axial vector and $\underline{\mathbf{I}}$ is the second-rank identity tensor. The skew operation creates a skew symmetric matrix from an axial vector (Mase *et al.*, 2010). The axial vector $\boldsymbol{\varphi}$ is related to the continuum scale curvature $\underline{\boldsymbol{\kappa}}$ present in the lattice:

$$\nabla\boldsymbol{\varphi} = \underline{\boldsymbol{\kappa}}. \tag{15}$$

In this model, the relationship between $\boldsymbol{\varphi}$ and $\underline{\boldsymbol{\kappa}}$ during heterogeneous single slip is more easily expressed in a coordinate system ($\mathbf{x}^{SS}$, $\mathbf{y}^{SS}$, $\mathbf{z}^{SS}$) defined by the slip direction, $\hat{\mathbf{s}}_{\mathbf{0}}$, the slip plane normal, $\hat{\mathbf{n}}_{\mathbf{0}}$, and their cross product, $\hat{\mathbf{t}}_{\mathbf{0}}$, prior to deformation. The rectangular Cartesian coordinate system is chosen such that $\mathbf{x}^{SS}$ lies along $\hat{\mathbf{s}}_{\mathbf{0}}$, $\mathbf{y}^{SS}$ lies along $\hat{\mathbf{n}}_{\mathbf{0}}$ and $\mathbf{z}^{SS}$ lies along $\hat{\mathbf{t}}_{\mathbf{0}}$. During single slip, a gradient of slip along the slip direction causes the curvature tensor to only have one nonzero component in the slip system coordinate system, κ_{zx}^{SS} (Nye, 1953):

$$\frac{\partial}{\partial x}(\varphi_z^{SS}) = \kappa_{zx}^{SS} \neq 0, \tag{16}$$

which means that the crystal orientation varies only in the slip direction, with different regions of the crystal rotating about $\hat{\mathbf{t}}_{\mathbf{0}}$ by varying amounts. Fig. 4 shows an exaggerated schematic of the process. In Fig. 4(*a*), a set of four mosaic blocks, initially with the same orientation, is shown. The straight lines in the mosaic blocks indicate the orientation of the slip plane. Heterogeneous slip causes each mosaic block to shear by varying amounts (Fig. 4*b*). The incompatibility of the lattice then causes misorientation to develop (Fig. 4*c*). Since φ_z^{SS} is the only nonzero component of $\boldsymbol{\varphi}$ in the slip system coordinate system, it subsequently will be referred to only as a scalar φ, dependent only on p_x^{SS}.

When building virtual mosaic crystals, the volume size of a mosaic block is chosen so that lattice misorientation between neighboring blocks is less than

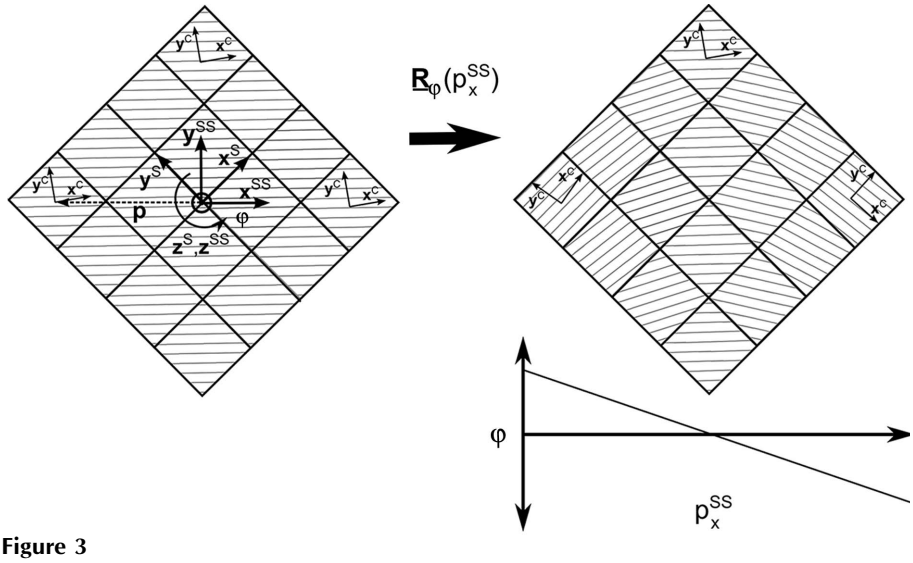

Figure 3
A two-dimensional illustration of the application of a distortion profile to a virtual mosaic crystal. The sample coordinate system is defined by $\mathbf{x}^S$, $\mathbf{y}^S$ and $\mathbf{z}^S$, a coordinate system associated with the deforming slip system is defined by $\mathbf{x}^{SS}$, $\mathbf{y}^{SS}$ and $\mathbf{z}^{SS}$, and the local crystal coordinate system of a mosaic block is defined by $\mathbf{x}^C$, $\mathbf{y}^C$ and $\mathbf{z}^C$. The position, $\mathbf{p}$, of the mosaic block is a vector from the sample origin to the mosaic block centroid. The orientation matrix, $\underline{\mathbf{R}}_{\varphi}$, rotates each mosaic block by angle φ according to its position along the slip direction, p_x^{SS}.

the minimum angular resolution of the detector employed [pixel size/$D_{max}(\tan 2\theta)$]. This ensures the distribution of intensity of the diffraction peaks will be continuous from the deformed crystals. In addition, the blocks are sufficiently small so that kinematic diffraction still applies. Care must be taken when using this model to simulate diffraction from large crystals. Mosaic models are poor for modeling diffraction of large perfect crystals prior to deformation and during small elastic deformations since dynamic diffraction effects will rapidly attenuate the incoming beam and change the direction of beam propagation within the crystal (Authier, 2001; Yan & Noyan, 2006). However, in this work it is assumed that heterogeneous lattice reorientation, caused by plastic deformation of the modeled crystals, is sufficient to reduce the long-range order of the crystals so that dynamic diffraction effects can be ignored (White, 1950).

Fig. 3 shows a schematic of how orientation distributions are applied to the virtual mosaic crystals. The lattice orientation of each mosaic block in the crystal is initially instantiated as a single chosen orientation, $\underline{\mathbf{R}}_{\mathbf{0}}^{S,C}$, and then is perturbed by position-dependent rotations, $\underline{\mathbf{R}}_{\varphi}(\mathbf{p})$, consistent with single slip as described previously. Since each mosaic block is rotating about $\hat{\mathbf{t}}_{\mathbf{0}}$ by the angle φ, equation (14) reduces to

$$\underline{\mathbf{R}}_{\varphi} = \underline{\mathbf{I}} + \varphi\,\mathrm{skew}(\hat{\mathbf{t}}_{\mathbf{0}}). \tag{17}$$

The relationships between the angle φ by which each mosaic block is rotated and p_x^{SS} are functions that can be varied to give the slip plane different curvatures. In this work, a linear relationship between φ and p_x^{SS}, consistent with edge dislocations uniformly distributed across the slip plane, is used.

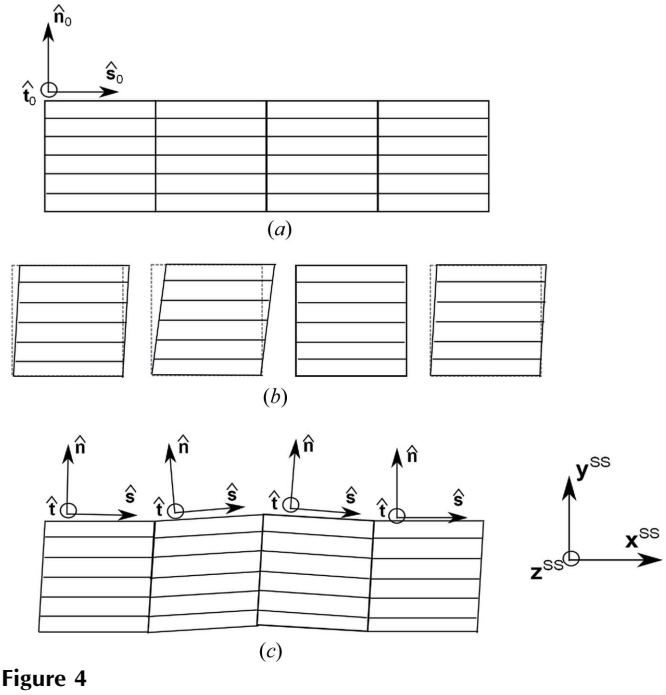

Figure 4
An exaggerated two-dimensional illustration of the relationship between inhomogeneous single slip and an orientation gradient developing in the crystal according to the Nye model (Nye, 1953). (*a*) A set of four undeformed mosaic blocks. (*b*) Heterogeneous slip causes each mosaic block to shear by a different amount. (*c*) Incompatibility causes an orientation gradient to develop.

3.2. Generating synthetic diffraction images

Once the virtual mosaic crystals are created, rotating crystal diffraction simulations are conducted on the virtual crystals to generate synthetic diffraction images. The exact parameters of the simulations, X-ray energy, beam size, detector type and distance, are set to match the experiment conducted. Each pixel of the detector is modeled as a bounded square region on a flat plane in space. A pixel records a 'count' when a diffracted X-ray intersects the detector plane within the pixel. The only modeled instrument broadening is the detector point-spread function. The point-spread function is modeled as a radial Lorentzian function with parameters set to match the detector employed.

The first step to generate synthetic diffraction images is to determine the diffractometer angles, ω, when diffraction events from each mosaic block will occur. Using equations (2), (3), (5) and (8), equation (6) can be reduced to

$$\cos(\omega)g_z^S - \sin(\omega)g_x^S - \frac{\lambda\|\mathbf{g}^S\|^2}{4\pi} = 0. \tag{18}$$

The roots (ω) of this equation are used to build a list of diffraction events (ω positions) from all reciprocal-lattice vectors.

To simulate rotating the crystal through $\Delta\omega$ as the detector is collecting intensity, all diffraction events from different mosaic blocks within $\Delta\omega$ are compiled into a list. The mosaic block positions during the diffraction event are then checked to ensure that the blocks are illuminated by the beam in the $\Delta\omega$ interval. If not, the diffraction events are removed from the list. The intersections, $\boldsymbol{\xi}$, of the diffracted beams with the detector surface (see Fig. 1*b*) are calculated for all diffraction events in the interval using equation (11). The intersection points are then used to determine which pixels on the detector record counts. Neighboring pixels record fractions of a count according to the point spread function of the detector. After all diffraction events in the rotation interval have been processed, pixel count values are rounded to the nearest integer and read out to generate a diffraction image. The Lorentz, polarization and temperature factors, which mainly change the magnitude of the diffracted intensity from different sets of lattice planes, are not included in the framework because the primary focus of this study was the effects of misorientation on the intensity distribution evolution within diffraction peaks, not the absolute magnitude of the intensity.

4. Identifying slip system activity using the simulation framework

4.1. *In situ* diffraction measurements of plastically deforming silicon

An *in situ* rotating crystal diffraction experiment was conducted on a silicon single crystal as it plastically deformed by dislocation glide at the A2 station of CHESS. Silicon was

Table 1
Schmid factors of the 12 primary slip systems of a silicon single-crystal specimen when the [123] direction is along the loading axis.

$\mathbf{s}_0$	$\mathbf{n}_0$	m
101	$1\bar{1}\bar{1}$	0.47
$\bar{1}01$	111	0.35
110	$1\bar{1}\bar{1}$	0.35
011	$1\bar{1}1$	0.28
$01\bar{1}$	111	0.17
110	$1\bar{1}1$	0.17
$1\bar{1}0$	111	0.17
$\bar{1}01$	$1\bar{1}1$	0.12
$01\bar{1}$	$1\bar{1}\bar{1}$	0.12
$1\bar{1}0$	$\bar{1}\bar{1}1$	0
101	$\bar{1}\bar{1}1$	0
011	$\bar{1}\bar{1}1$	0

used because of the availability of large single crystals with low defect concentration and its well characterized macroscopic mechanical properties. Plastic deformation was initiated by applying a uniaxial compressive stress along $\mathbf{y}^S$ with the crystal heated to 1073 K. The sample was heated to 1073 K because silicon is brittle at room temperature, but above 973 K becomes increasingly ductile, and measurable macroscopic plastic deformation will occur prior to fracture (Alexander & Haasen, 1969). The sample was cut from a float-zone-grown silicon boule to be oriented for single slip using a diamond blade saw and then etched for stress relief. After etching, the sample size was 0.80 × 2.20 × 0.80 mm along $\mathbf{x}^S$, $\mathbf{y}^S$ and $\mathbf{z}^S$. The crystal was illuminated by a 50 keV monochromatic X-ray beam with a beam size of 0.75 × 0.75 mm. The detector used was a GE41RT+ amorphous silicon area detector with 2048 × 2048 pixels and 200 × 200 µm pixel size sitting a distance of 1020 mm from the sample. Note that because of the large size of both the crystal and the beam, at the onset of plastic deformation, the detector is in the intermediate field of Fig. 2, where $\Delta\eta \simeq \|\mathbf{p}\|$, so effects from both the topology of the crystal and the distribution of lattice orientation should be present and of similar magnitude.

When the resolved shear stress on a crystal slip system reaches the critical resolved shear stress, τ_{CRSS}, dislocation glide begins. The resolved shear stress on a slip system, τ, is determined using the transformation

$$\tau = \hat{\mathbf{s}}_0 \cdot \underline{\boldsymbol{\sigma}} \hat{\mathbf{n}}_0, \tag{19}$$

where $\underline{\boldsymbol{\sigma}}$ is the macroscopic stress tensor. The ratio of resolved shear stress on a slip system to the uniaxial stress applied is the Schmid factor m:

$$m = \left|\tau/\sigma^S_{yy}\right| = \left|\hat{\mathbf{s}}^S_{0y}\hat{\mathbf{n}}^S_{0y}\right|. \tag{20}$$

During uniaxial loading, the Schmid factor of a slip system depends only on the orientation of the slip direction and slip normal. As the macroscopic stress is increased, the Schmid factor dictates which slip system should activate first. The silicon crystal was manufactured so that the [123] crystallographic direction lies along the loading axis in order to produce single slip at the elastic–plastic transition. The primary slip systems of silicon at 1073 K are of the ⟨110⟩{111} type, so $\mathbf{x}^{SS}$ lies along ⟨110⟩ directions, $\mathbf{y}^{SS}$ along ⟨111⟩ directions and $\mathbf{z}^{SS}$ along ⟨211⟩ directions (Alexander & Haasen, 1969). Table 1 lists the Schmid factors of the 12 primary slip systems in silicon when the crystal is oriented with the [123] direction along the loading axis. Aligning the [123] crystallographic direction with the loading axis maximizes the ratio between the two largest Schmid factors, ensuring that if the crystal has been manufactured and loaded correctly, dislocation glide should initially occur on one crystallographic plane, ideal for comparison with the single-slip mosaic crystal model used in this work.

The sample was heated to 1073 K with a small compressive preload (−5 MPa) applied to maintain stability. The sample was heated using a resistance wire furnace with the temperature maintained by proportional–integral–derivative (PID) control. The diffractometer, load frame and furnace used in the experiment are described in detail by Oswald *et al.* (2013). Once 1073 K was reached, diffraction peaks were measured from different sets of lattice planes by rotating the crystal about $\mathbf{y}^L$ as the detector collected intensity ($\Delta\omega = 1°$). The compressive stress was then increased to −20 MPa, sufficient to initiate plastic deformation (Siethoff, 1999), and then unloaded to −18 MPa (90% of the maximum stress magnitude). By reducing the applied stress, the loading point was relaxed from the single-crystal yield surface, slowing the evolution of the lattice state due to creep during the measurement of diffraction peaks. If a diffraction peak spanned more than one image, the intensities were summed in post-processing.

Fig. 5 shows 12 diffraction peaks measured across the available rotation range of the diffractometer before and after plastic deformation. Since the diffraction peaks occur at different radial and azimuthal positions on the detector, the azimuthal (η) width of one pixel varies from peak to peak. These values are included at the top of the figure for reference. Not all available diffraction peaks were measured in order to reduce data collection time and

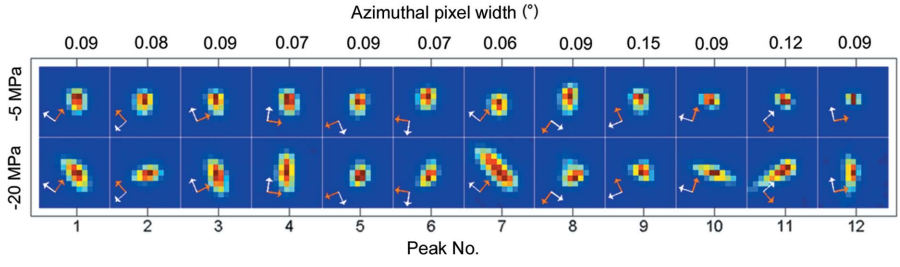

Figure 5
Diffraction peaks measured *in situ* from the [123] silicon single crystal before (−5 MPa) and after plastic deformation (−20 MPa) at 1073 K. Orange arrows indicate the radial direction on the detector and white arrows indicate the azimuthal direction. The azimuthal angular widths of one pixel for each diffraction peak are included for scale.

Table 2
The Miller indices and associated angles for the diffraction peaks in Figs. 5 and 6.

Peak No.	h	k	l	2θ (°)	η (°)	ω (°)
1	$\bar{1}$	1	3	8.66	55.17	−39.5
2	3	3	1	11.39	133.36	−38.5
3	$\bar{2}$	0	2	7.38	23.50	−35.5
4	$\bar{3}$	$\bar{1}$	1	8.66	351.90	−35.5
5	2	0	$\bar{2}$	7.38	203.43	−27.5
6	3	1	$\bar{1}$	8.66	171.91	−26.5
7	$\bar{2}$	2	4	12.80	51.59	−26.5
8	1	$\bar{1}$	$\bar{3}$	8.66	235.08	−24.5
9	1	1	1	4.52	113.45	−24.5
10	0	2	2	7.38	72.41	21.5
11	$\bar{2}$	0	$\bar{2}$	7.38	311.97	24.5
12	$\bar{2}$	2	0	7.38	12.19	26.5

prevent lattice state evolution during data collection. The Miller indices and diffractometer angles of the peaks are given in Table 2. The slight broadening of the diffraction peaks prior to deforming the sample is believed to be due to small amounts of sample evolution due to creep at 1073 K from the applied preload. Significant evolution of the diffraction peak widths in the azimuthal direction is observed during deformation. As expected, the evolution is very non-uniform across all peaks.

4.2. Simulation of experiment and comparison with experimental results

The feasibility of using the diffraction peaks predicted by the simulation framework as an indicator of slip system activity was examined by comparing simulated peaks from different virtual crystals with the experimental data seen in Fig. 5. To compare with the experiment, virtual silicon samples were generated that all had $\underline{\mathbf{R}}_0^{S,C}$ equal to the initial orientation of the experimental crystal. Each of the three slip systems with the highest Schmid factors (see Table 1) was deformed with either a positively or a negatively sloped linear orientation gradient, for a total of six virtual crystals. Reversing the slope of orientation gradients is equivalent to changing the concavity of slip planes or reversing the direction of Burger's vector of the geometrically necessary dislocations within the mosaic crystals. *A priori* there is no knowledge of whether the slip plane in the experiment developed positive or negative concavity, so both possibilities are simulated. Reversing the concavity will produce markedly different diffraction evolution when the detector is in the intermediate field, which will be revisited in the *Discussion*.

The experimental geometry and detector were modeled to match conditions at the A2 station at CHESS. The point-spread function of the detector is modeled as a radial Lorentzian function with parameters set to match the detector used in the A2 station (M. Tate, 2011, unpublished). The magnitude of the misorientation for this set of virtual crystals was 0.8° to be comparable to the misorientation measured in the experimental data. The virtual sample size was 0.80 × 0.75 × 0.80 mm along $\mathbf{x}^S$, $\mathbf{y}^S$ and $\mathbf{z}^S$. The dimension along $\mathbf{y}^S$ was chosen to match the beam height, while the other two dimensions match the experimental specimen. Each virtual crystal had approximately 15 000 equally spaced mosaic blocks per mm^3 (30 per mm along $\mathbf{x}^S$, $\mathbf{y}^S$ and $\mathbf{z}^S$), which was sufficient to generate continuous diffraction peaks. The basis vector magnitudes are equal to the lattice parameter of silicon at 1073 K (5.44 Å; Okada & Tokumaru, 1984).

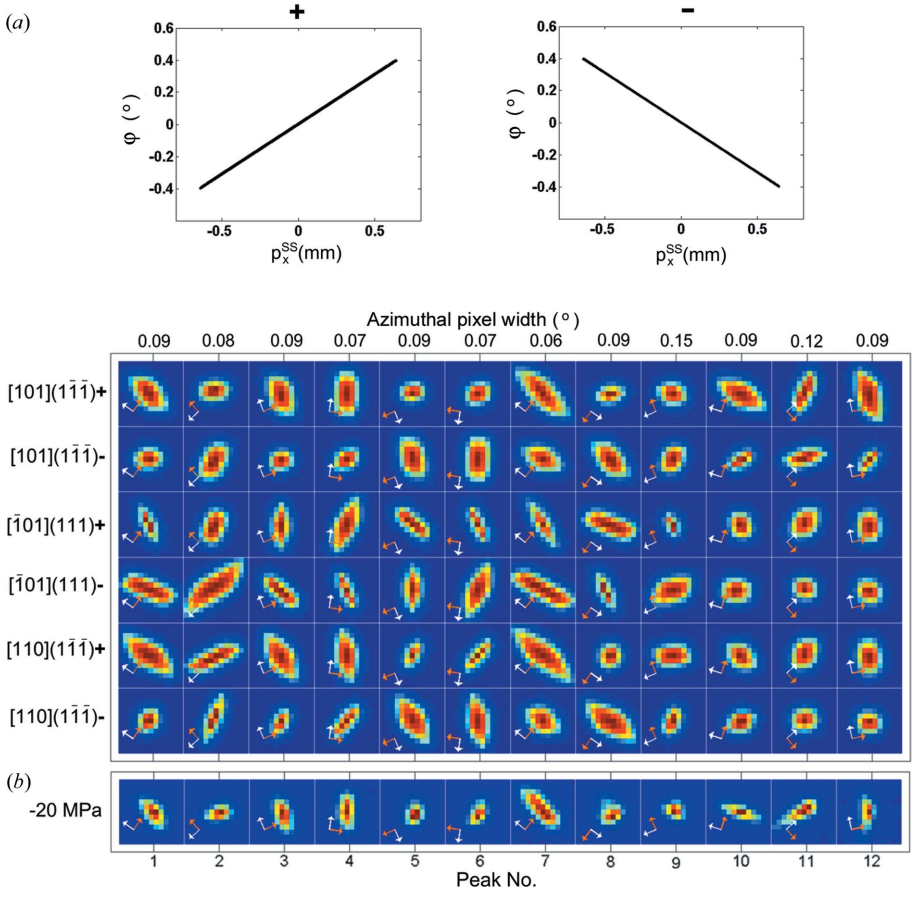

Figure 6
(*a*) Diffraction peaks from six deformed virtual silicon single crystals. The initial mosaic block crystal orientation, $\underline{\mathbf{R}}_0^{S,C}$, of the six virtual crystals matches the initial [123] crystal orientation of the silicon crystal deformed in the experiment. The three slip systems with the highest resolved shear stresses were deformed using linear distortion profiles with opposite slip plane concavities, denoted + and −, respectively, in the upper view. (*b*) The experimentally measured diffraction peaks after plastic deformation are included from Fig. 5 to enable visual comparison. Orange arrows indicate the radial direction on the detector, and white arrows indicate the azimuthal direction. The azimuthal angular widths of one pixel for each diffraction peak are included for scale.

Fig. 6(*a*) shows the simulated diffraction peaks from the six virtual crystals, three slip systems with the two orientation gradients applied to each. At the top of Fig. 6(*a*), the simulated relationships between φ and p_x^{SS} are shown. Fig. 3 can be used as a reference for how the orientation gradients are applied. The experimentally measured diffraction peaks after plastic deformation are shown again in Fig. 6(*b*) to enable comparison. By observing Fig. 6(*b*), the large differences in the magnitudes of the azimuthal peak width between sets of diffraction peaks from different virtual crystals can be seen. Changes due to differences in deformed slip system and slip plane concavity have given each set of peaks its own distinct 'signature'. The crystal denoted $[101](1\bar{1}\bar{1})+$ has the best qualitative visual agreement between the simulation and experiment across the set of diffraction peaks, which was expected since the $[101](1\bar{1}\bar{1})$ slip system had the highest Schmid factor. There is very good agreement between which peaks substantially broaden azimuthally and which do not, indicating that the $[101](1\bar{1}\bar{1})$ slip system was active. Also, at the intermediate sample-to-detector distance, explored in both the experiment and the simulation, it is also possible to discern the sign of the slip plane concavity because of the large difference in diffraction peaks between $[101](1\bar{1}\bar{1})+$ and $[101](1\bar{1}\bar{1})-$.

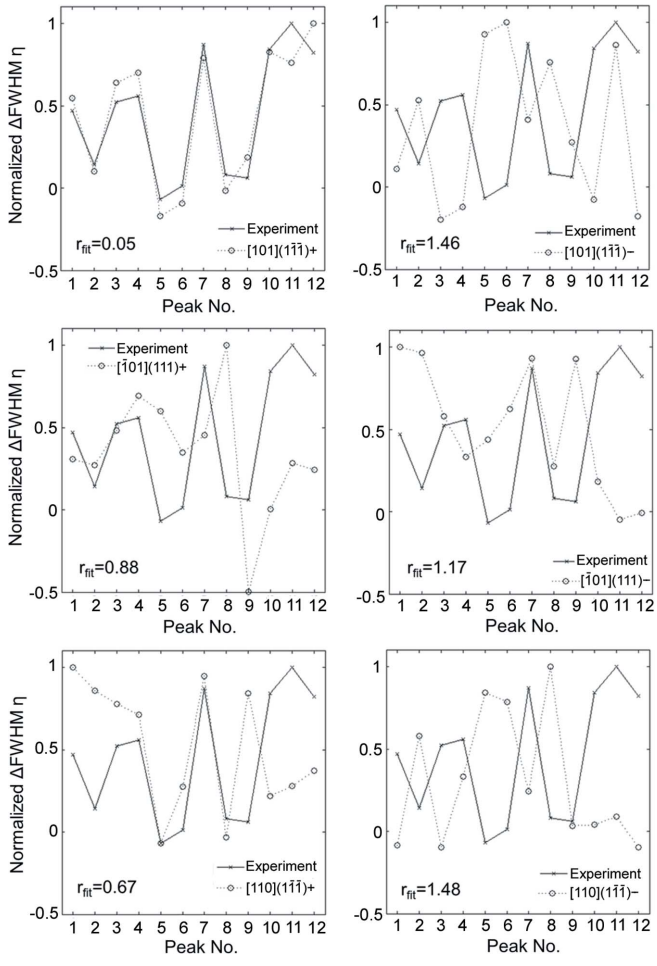

Figure 7
Normalized $\Delta\text{FWHM}\eta$ of the diffraction peaks from the six deformed virtual silicon crystals shown in Fig. 6. Overlaid is the $\Delta\text{FWHM}\eta$ from the experimentally measured diffraction peaks in Fig. 5. Also shown are the r_{fit} values quantitatively comparing the $\Delta\text{FWHM}\eta$ of the diffraction peak sets.

Fig. 6 presents compelling visual evidence that the model is capturing the deformation-induced peak evolution associated with single slip. However, to systematically quantify the azimuthal broadening of the diffraction peaks, the intensity distribution of each diffraction peak is integrated in the radial direction, giving a one-dimensional profile of intensity as a function of the azimuthal angle, η, on the detector:

$$I_{hkl}(\eta) = \int I_{hkl}(2\theta, \eta)\, \mathrm{d}2\theta. \tag{21}$$

The diffraction peaks are integrated as described by Schuren & Miller (2011) with modifications to allow for radial integrations. The full width at half-maximum (FWHM) of $I_{hkl}(\eta)$ is then used as a quantitative evolution measure. To mitigate the effects of the initial peak width, the change in the azimuthal FWHM ($\Delta\text{FWHM}\eta$) from the initial state is used to examine differences in the peak broadening between crystals. It should be mentioned that the large pixel size of the GE detector introduces subpixel-sized uncertainty in the FWHM measurements. However, as can be seen in Fig. 5, the changes in azimuthal peak width before and during loading are substantial, with some peaks more than doubling in size. Since the analysis is only looking at large changes in peak widths, the uncertainty introduced by the pixel size should not affect the analysis. In order to compare the evolution of the diffraction peaks from crystals with different misorientation magnitudes, the $\Delta\text{FWHM}\eta$ values are normalized by the maximum $\Delta\text{FWHM}\eta$ value of each crystal's diffraction peak set. A value of one corresponds to the largest change in azimuthal peak width across a set of diffraction peaks from a single crystal, zero corresponds to no peak width evolution and a negative value is a decrease in azimuthal peak width. Fig. 7 shows the normalized $\Delta\text{FWHM}\eta$ of the simulated diffraction peaks against the experimentally measured change. The quantitative measure confirms what could be visually observed. The $[101](1\bar{1}\bar{1})+$ virtual crystal captures most of the major diffraction peak evolution trends of the experimental data, including the narrowing of peaks 5 and 6, that the other simulated crystals did not capture. Lastly, a simple 'goodness-of-fit' parameter, r_{fit}, can be calculated to determine which virtual crystal best agrees with the experimental data without having to make visual comparisons:

$$r_{fit} = \frac{\sum_{i=1}^{PKS}\left(\Delta\text{FWHM}\eta_i^{exp} - \Delta\text{FWHM}\eta_i^{sim}\right)^2}{\sum_{i=1}^{PKS}\left(\Delta\text{FWHM}\eta_i^{exp}\right)^2} \tag{22}$$

where PKS is the total number of peaks. The r_{fit} values for each virtual crystal in comparison to the experimental data are also listed in Fig. 7. The r_{fit} value for the $[101](1\bar{1}\bar{1})+$ crystal is significantly lower than those for the other virtual crystals,

which gives confidence that the model is correctly identifying the active slip system.

5. Discussion

5.1. Identifying slip system activity in intermediate- and far-field HEDM experiments

We have presented results for identifying slip activity within an initially perfect single crystal during single-slip conditions. As seen, the key to this method is the existence and generation of the characteristic diffraction peak evolution using forward modeling, which can then be compared with experimental results. Virtual crystals, modeled as collections of mosaic blocks, were generated with orientation gradients present, consistent with a model of heterogeneous single slip on different slip systems. Diffraction simulations showed characteristic azimuthal diffraction peak evolution that could be associated with each slip system. The characteristic diffraction peak evolution was compared with *in situ* experimental results from a single crystal oriented for single slip. From the comparisons, the active slip system was correctly identified. The intermediate-field position of the detector complicated analysis since each slip system required simulation of both positive and negative concavity of the slip plane. This extra step in the analysis is a result of the contributions to the diffracted intensity distribution from both the real-space topology and the distribution of orientation being of comparable magnitudes in the intermediate field. In the far field, this step would not be necessary since the distribution of orientation would dominate the diffracted intensity. Fig. 8 illustrates these statements. In Fig. 8, a schematic is shown of how reversing an orientation gradient, equivalent to switching the slip plane concavity or changing the Burger's vector sign of the GND distribution within the crystal, can affect azimuthal peak evolution. In Fig. 8, the two sets of mosaic blocks shown have reversed orientation gradients, and the diffraction peaks from both distributions are shown in both intermediate- ($\|\Delta\mathbf{p}\| \simeq \eta$) and far-field ($\|\Delta\mathbf{p}\| >> \eta$) geometries.

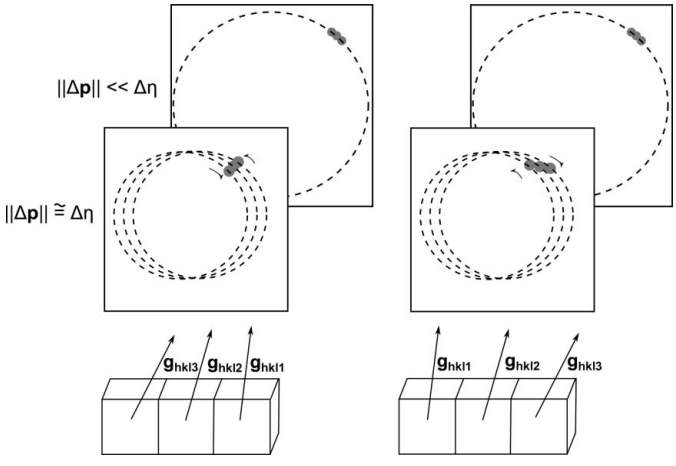

Figure 8
A schematic depicting two mosaic crystals containing the same distribution of orientations but with the orientations spatially varied in two different manners. The effects on the diffraction peak evolution in the intermediate- and far-field geometries are both shown.

Reversing the ordering of the first and last crystals causes the diffracted intensity distribution to either shrink or broaden azimuthally in the intermediate detector configuration. On the far-field detector, the differences between these two orientation configurations, shown in Fig. 8, are no longer observed. Referring back to Fig. 2, the collapse of the diffraction peaks from the individual mosaic blocks to a single arc in the far field causes the diffracted intensity from both mosaic crystals to appear to broaden azimuthally. This indicates that the slip system activity analysis presented in this work would be simplified in the far field. Each slip system would only require a single simulation to generate the characteristic azimuthal peak evolution; however, spatial information about the orientation distribution (and the GND distribution) is lost. Therefore when conducting these experiments, the geometry must be considered when determining whether only slip system activity or slip system activity and slip plane concavity are of interest.

5.2. Application of model to slip system activity in polycrystals

The work presented analyzed the deformation of a single crystal; however, the general procedure can be extended to analyzing slip system activity within deforming grains in a polycrystal. The analysis requires that the number of grains illuminated is small enough (<1000) so that diffraction peaks from individual grains can be resolved rather than full powder rings. In addition, the geometry can be in either the intermediate- or the far-field geometry, depending on whether or not the experimenter wishes to identify slip plane concavity. Note that grains in a polycrystal are significantly smaller than the diffraction volume probed in this work; therefore the detector must be significantly closer to the sample to be in an intermediate-field geometry ($D \simeq 150$ mm for 50–100 μm grain size). The intermediate geometry gives the benefit of being able to determine the sign of unpaired dislocations causing the lattice curvature, which the far-field geometry can not resolve, as seen in Fig. 8. However, the far-field geometry simplifies analysis by halving the number of virtual crystals required since only a single orientation gradient must be applied for each slip system. A procedure for investigating slip system activity within polycrystals is given below. The procedure closely mimics the work presented in this paper, with small changes made to account for differences in experiment:

(*a*) Conduct a rotating crystal diffraction experiment with the detector in the intermediate or far field.

(*b*) Identify peaks associated with a grain of interest: ideally, more than ten peaks spread over a wide range of η and ω angles.

(*c*) Determine the grain's orientation, average stress state and volume from the diffraction data.

(*d*) Determine the ΔFWHMη for the measured diffraction peaks.

(*e*) Build a list of candidate slip systems. If τ_{CRSS} is known for the candidate slip systems, knowledge of the stress state can be used to reduce the number of candidate slip systems to those with sufficient τ to be active.

(*f*) Generate a virtual grain for each possible slip system with volume and initial orientation equivalent to the grain being examined.

(*g*) Apply orientation gradients with magnitudes comparable to the measured misorientation to the virtual crystals. (1) Intermediate geometry: apply positive and negative linear orientation gradients to each slip system; (2) far-field geometry: apply a positive or negative linear orientation gradients to each slip system.

(*h*) Conduct virtual diffraction experiments on the virtual crystals and use the $\Delta\mathrm{FWHM}\eta$ of the diffraction peaks to find the characteristic azimuthal evolution for activity on each candidate slip system.

(*i*) Find the r_{fit} for each candidate slip system in comparison to the experimental data.

Further work is required to determine how low the r_{fit} value must be in order to have sufficient confidence that the active slip system is being properly identified. However, from the results in §4, r_{fit} must be significantly below 0.5 since an inactive slip system had an r_{fit} of 0.67.

5.3. Model limitations and future work

The current work analyzed the effects of a single active slip system on diffraction peak evolution. Further investigation is required to determine whether the presented diffraction peak analysis can be applied to crystals deforming by polyslip. The first-order commutative property of addition of small rotations indicates that superposition of orientation gradients consistent with single slip may be possible for analyzing peak broadening due to polyslip during early plastic deformation. However, extension of the modeling approach presented to polyslip conditions would require specifying relative degrees of slip system activity. One method would be to assume that the effects of slip system activity could be superimposed, which is reasonable for the small amount of misorientation near the elastic–plastic transition. The changes in $\Delta\mathrm{FWHM}\eta$ from each slip system could then be combined to find a best fit to the data. A minimization of the following function, *f*, could be used to find the relative activities (α_j):

$$f(\alpha_j) = \sum_{i=1}^{\mathrm{PKS}} \left(\Delta\mathrm{FWHM}\eta_i^{\mathrm{exp}} - \sum_{j=1}^{\mathrm{SS}} \alpha_j \Delta\mathrm{FWHM}\eta_{ij}^{\mathrm{sim}} \right)^2, \qquad (23)$$

where $\sum \alpha_j = 1$. The number of possible slip systems (SS) should be reduced to only those where $\tau > \tau_{\mathrm{CRSS}}$ to simplify the minimization, since the average stress state of a crystal can be measured.

This paper focused on a methodology for identifying slip system activity in crystals during the elastic–plastic transition, which is of practical importance for understanding fatigue and fracture in engineering applications. As crystals begin to enter fully developed plasticity with five active slip systems and misorientation magnitudes larger than several degrees, the methodology presented in this paper will, most likely, break down. First, as the deformation increases and the misorientation grows, the diffracted intensity will quickly become dominated by the misorientation present, making placing the detector close enough to be in an intermediate configuration difficult. Also, as the deformation increases and the crystals develop dislocation structures, the linear orientation gradients applied to the crystals will no longer be a good approximation for the crystal's deformation. More complicated models that evaluate full sets of field equations will be necessary to generate these complicated orientation distributions. Lastly, the rotating crystal method employed introduces ambiguity in the relationship between lattice misorientation and diffraction peak evolution because of the dimensionality loss in the measurements due to integration (collecting intensity as the diffractometer rotates). To address some of the ambiguity in the interpretation of diffraction peak deformation, the angular width ($\Delta\omega$) of the collection interval in the rotating crystal method should be reduced to allow for the construction of single-crystal pole figures and reciprocal-space maps (Fewster, 1997; Jakobsen *et al.*, 2006). The single-crystal pole figures are two-dimensional projections of the orientation distribution present in the mosaic crystal, rather than the one-dimensional azimuthal evolution on an area detector used in this work. These single-crystal pole figures can subsequently be used to determine orientation distribution functions within the crystal, giving more complete pictures of the distribution of the lattice state (Hansen *et al.*, 2009; Barton & Bernier, 2012). Unambiguous orientation space distributions show promise for making analysis of slip activity during fully developed plasticity significantly more tractable than the forward projection method presented.

6. Summary and conclusions

In this work, it is shown that the orientation gradients assumed to be present in crystals plastically deformed by single slip are consistent with Nye's model of heterogeneous single slip at the onset of plastic deformation. 'Deformed' virtual crystals were generated by applying orientation gradients consistent with a simple model of heterogeneous single slip. The diffraction peaks from a deformed virtual crystal and the diffraction peaks measured *in situ* from a plastically deformed silicon single crystal showed very good agreement, both qualitatively by visual observation and quantitatively by measures of changes of the azimuthal diffraction peak widths. Both the axis about which the mosaic crystal develops misorientation and the topology of the mosaic blocks were shown to play a large role in the distribution of intensity measured on an area detector in the intermediate-field geometry employed. The axis about which a crystal develops misorientation is related to the active slip system and the topology of the mosaic blocks is related to the concavity of the slip plane. The close comparison between the experimental and simulated results demonstrates that the present model can be used to identify slip system activity in monochromatic X-ray diffraction experiments.

The work presented in this paper was supported financially by the National Science Foundation (NSF) under award No. CMMI-0928257 (Dr Glaucio Paulino program manager). Experiments using the system were conducted at the Cornell High Energy Synchrotron Source (CHESS), which is supported by the National Science Foundation and the National Institutes of Health/National Institute of General Medical Sciences under NSF award No. DMR-0936384. DCP is supported by a GRA position at CHESS. The authors wish to thank Mark Obstalecki for help performing the silicon compression experiment and Dr Darren Dale for his support as staff scientist at the A2 station at CHESS during this work.

References

Alexander, H. & Haasen, P. (1969). *Solid State Physics*, Vol. 22, pp. 27–158. New York: Academic Press.
Als-Nielsen, J. & McMorrow, D. (2011). *Elements of Modern X-ray Physics*, 2nd ed. Chichester: Wiley.
Arsenlis, A. & Parks, D. (1999). *Acta Mater.* **47**, 1597–1611.
Authier, A. (2001). *Dynamical Theory of X-ray Diffraction*, 2nd ed. Oxford University Press.
Barabash, R., Ice, G. E., Larson, B. C., Pharr, G. M., Chung, K.-S. & Yang, W. (2001). *Appl. Phys. Lett.* **79**, 749–751.
Barabash, R. I., Ice, G. E. & Walker, F. J. (2003). *J. Appl. Phys.* **93**, 1457–1464.
Barton, N. R. & Bernier, J. V. (2012). *J. Appl. Cryst.* **45**, 1145–1155.
Bernier, J. V., Barton, N. R., Lienert, U. & Miller, M. P. (2011). *J. Strain Anal. Eng. Des.* **46**, 527–547.
Busing, W. R. & Levy, H. A. (1967). *Acta Cryst.* **22**, 457–464.
Cahn, R. (1950). *Prog. Metal Phys.* **2**, 151–176.
Darwin, C. (1914). *Philos. Mag. Ser. 6*, **27**, 675–690.
Fewster, P. F. (1997). *Crit. Rev. Solid State Mater. Sci.* **22**, 69–110.
Gonzalez, D., King, A., Mostafavi, M., Reischig, P., du Roscoat, S. R., Ludwig, W., da Fonseca, J. Q., Withers, P. & Marrow, T. (2013). *Acta Mater.* **61**, 7521–7533.
Hansen, P., Sørensen, H., Süküsd, Z. & Poulsen, H. (2009). *SIAM J. Imaging Sci.* **2**, 593–613.
Hofmann, F., Keegan, S. & Korsunsky, A. (2012). *Mater. Lett.* **89**, 66–69.
Ice, G. & Barabash, R. (2007). *Dislocations in Solids*, Vol. 4, pp. 261–362. Amsterdam: Elsevier.
Jakobsen, B., Poulsen, H., Lienert, U., Almer, J., Shastri, S., Sørensen, H., Gundlach, C. & Pantleon, W. (2006). *Science*, **312**, 889–892.
Joffe, A. & Kirpitcheva, M. (1922). *Philos. Mag. Ser. 6*, **43**, 204–206.
Johnson, G., King, A., Honnicke, M. G., Marrow, J. & Ludwig, W. (2008). *J. Appl. Cryst.* **41**, 310–318.
Korsunsky, A., Hofmann, F., Abbey, B., Song, X., Belnoue, J., Mocuta, C. & Dolbnya, I. (2012). *Int. J. Fatigue*, **42**, 1–13.
Li, S. F., Lind, J., Hefferan, C. M., Pokharel, R., Lienert, U., Rollett, A. D. & Suter, R. M. (2012). *J. Appl. Cryst.* **45**, 1098–1108.
Lienert, U., Brandes, M., Bernier, J., Weiss, J., Shastri, S., Mills, M. & Miller, M. (2009). *Mater. Sci. Eng. A*, **524**, 46–54.
Ludwig, W., Reischig, P., King, A., Herbig, M., Lauridsen, E. M., Johnson, G., Marrow, T. J. & Buffière, J. Y. (2009). *Rev. Sci. Instrum.* **80**, 033905.
Margulies, L., Lorentzen, T., Poulsen, H. & Leffers, T. (2002). *Acta Mater.* **50**, 1771–1779.
Mase, G., Smelser, R. & Mase, G. (2010). *Continuum Mechanics for Engineers*, 3rd ed. Boca Raton: CRC Press.
Nye, J. (1953). *Acta Metall.* **1**, 153–162.
Okada, Y. & Tokumaru, Y. (1984). *J. Appl. Phys.* **516**, 314–320.
Oswald, B., Schuren, J., Pagan, D. C. & Miller, M. P. (2013). *Rev. Sci. Instrum.* **84**, 033902.
Poulsen, H. (2004). *Three-Dimensional X-ray Diffraction Microscopy*, 1st ed. Berlin, Heidelberg: Springer.
Schuren, J. C. & Miller, M. P. (2011). *J. Strain Anal. Eng. Des.* **46**, 663–681.
Siethoff, H. (1999). *Properties of Crystalline Silicon*, pp. 122–135. London: Institution of Engineering and Technology.
Song, X., Hofmann, F. & Korsunsky, A. M. (2010). *Philos. Mag.* **90**, 3999–4011.
Suter, R. M., Hennessy, D., Xiao, C. & Lienert, U. (2006). *Rev. Sci. Instrum.* **77**, 123905.
Van Swygenhoven, H. & Petegem, S. (2010). *JOM*, **62**, 36–43.
Warren, B. E. (2004). *X-ray Diffraction*, 2nd ed. New York: Dover.
White, J. E. (1950). *J. Appl. Phys.* **21**, 855–859.
Wilkens, M., Ungár, T. & Mughrabi, H. (1987). *Phys. Status Solidi A*, **104**, 157–170.
Wong, S., Park, J., Miller, M. & Dawson, P. (2013). *Comput. Mater. Sci.* **77**, 456–466.
Yan, H. & Noyan, I. C. (2006). *J. Appl. Cryst.* **39**, 320–325.